ACS APPLIED MATERIALS & INTERFACES

Research Article

www.acsami.org

One-Step Facile Solvothermal Synthesis of Copper Ferrite−Graphene Composite as a High-Performance Supercapacitor Material

Wang Zhang,[†,‡] Bo Quan,[†,‡] Chaedong Lee,[†,‡] Seung-Keun Park,[†,‡] Xinghe Li,[†,‡] Eunjin Choi,[†,‡] Guowang Diao,*[,§] and Yuanzhe Piao*[,†,‡]

[†]Graduate School of Convergence Science and Technology, Seoul National University, Seoul 151-742, Republic of Korea

[‡]Advanced Institutes of Convergence Technology, Suwon 443-270, Republic of Korea

[§]College of Chemistry and Chemical Engineering, Yangzhou University, Yangzhou, 225002 Jiangsu, People's Republic of China

Supporting Information

ABSTRACT: In this work, we reported a facile approach to prepare a uniform copper ferrite nanoparticle-attached graphene nanosheet ($CuFe_2O_4$-GN). A one-step solvothermal method featuring the reduction of graphene oxide and formation of $CuFe_2O_4$ nanoparticles was efficient, scalable, green, and controllable. The composite nanosheet was fully characterized by X-ray diffraction (XRD), transmission electron microscopy (TEM), and X-ray photoelectron spectroscopy (XPS), which demonstrated that $CuFe_2O_4$ nanoparticles with a diameter of approximately 100 nm were densely and compactly deposited on GN. To investigate the formation mechanism of $CuFe_2O_4$-GN, we discussed in detail the effects of a series of experimental parameters, including the concentrations of the precursor, precipitation agent, stabilizer agent, and graphene oxide on the size and morphology of the resulting products. Furthermore, the electrochemical properties of the $CuFe_2O_4$-GN composite were studied by cyclic voltammetry and galvanostatic charge−discharge measurements. The composite showed high electrochemical capacitance (576.6 $F{\cdot}g^{-1}$ at 1 $A{\cdot}g^{-1}$), good rate performance, and cycling stability. These results demonstrated that the composite, as a kind of electrode materials, had a high specific capacitance and good retention. The versatile $CuFe_2O_4$-GN holds great promise for application in a wide range of electrochemical fields because of the remarkable synergistic effects between $CuFe_2O_4$ nanoparticles and graphene.

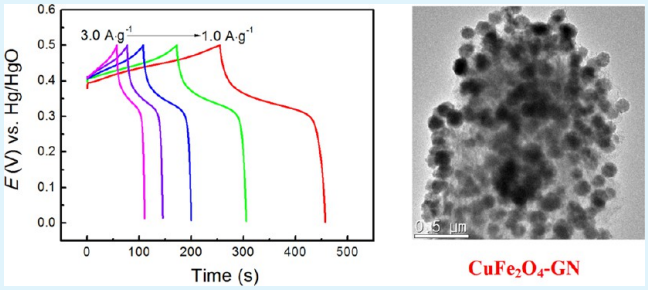

KEYWORDS: *$CuFe_2O_4$, graphene, solvothermal procedure, supercapacitor*

1. INTRODUCTION

Electrochemical capacitors have the potential to emerge as promising energy storage devices owing to the advantages of short charging times, a long cycle, and high power and energy density.[1−3] The crucial task for constructing an electrochemical capacitor is exploring an electrode material with high energy and power densities. Transition metal oxides have been proved favorable for supercapacitors.[4,5] For example, hydrous ruthenium dioxide ($RuO_2{\cdot}nH_2O$) has significant potential for the fabrication of advanced electrodes owing to its excellent properties, which include high theoretical specific capacitance (720 $F{\cdot}g^{-1}$) and high electrical conductivity.[6,7] However, the large-scale applications of $RuO_2{\cdot}nH_2O$ for supercapacitors are definitely hindered by its toxic nature, scarcity, and high cost. Hence, design of a desirable, low-cost electrode material with a longer cycling lifetime and higher energy density is imperative for electrochemical energy storage.[8]

Binary metal oxides, which exhibit good electrochemical performance, have been widely used in electrochemical applications, such as electrochemical capacitors,[9] Li-ion batteries,[10] fuel cells,[11,12] and solar cells.[13] Transition metal oxides with a general formula AB_2O_4 have a spinel crystal structure, which is very important for electrochemical capacitors, because it offers a robust crystalline architecture with three-dimensional diffusion pathways.[14] Currently, a number of spinel compounds have been investigated for electrochemical capacitors, including Fe_3O_4,[15] $MnFe_2O_4$,[16] and $NiCo_2O_4$.[17] $CuFe_2O_4$ with inverse spinel structure is one of the most important ferrites in transition metal oxides. Transition metal oxides have been widely used in electronics and catalysts in recent years owing to the advantages exhibited in these materials that include environmental compatibility, high catalytic activity, and easy separation.[18−20] Sreedhar et al. synthesized $CuFe_2O_4$ nanoparticles as a magnetically recoverable and reusable catalyst for the synthesis of 5-substituted 1*H*-tetrazoles.[21] Yen et al. reported a novel one-step-impregnation method to synthesize $CuFe_2O_4$ using mesoporous silica.[22] This method enabled a true replication of the mesostructure with

Received: October 13, 2014
Accepted: January 13, 2015
Published: January 13, 2015

DOI: 10.1021/am507014w
ACS Appl. Mater. Interfaces 2015, 7, 2404−2414

high yield and phase purity, while retaining the template morphology. As the anode for Li-ion batteries, carbon coated hollow $CuFe_2O_4$ spheres, which had a high specific capacity of 550 mA·h·g^{-1}, were prepared using a polymer-template hydrothermal growth method by Jin et al.[23] $CuFe_2O_4$ hollow fibers, which had a typical pseudocapacitive capacitance, were obtained by Zhao and his co-workers by electrospinning.[24] Previously, we also reported the formation and capacitance property of porous $CuFe_2O_4$ nanospheres.[25] Although $CuFe_2O_4$ has been regarded as a promising material for electrochemical capacitors because of its high theoretical capacity (895 mA·h·g^{-1}) and low cost,[23,26,27] its inherent poor conductivity is a negative factor that impedes its application in electrochemical capacitors.

Graphene is an intriguing two-dimensional carbon nanomaterial that is widely utilized to design fascinating electrode materials for supercapacitors because of its ultrathin nanostructure, excellent electrical conductivity, and mechanical stability.[28−30] Recently, researchers have reported on the application of graphene-based transition metal oxide composites as electrochemical materials.[31−36] The hybrid materials can improve electrochemical performance with the synergistic effect between graphene and transition metal oxides. In these systems, graphene has offered not only a conductive backbone to facilitate electron transport, but also a mechanical structure that maintains the integrity of the electrode during the electrochemical process.[37] In addition, graphene with metal oxide can be an economic and a promising way to achieve high supercapacitor performance.[38]

To overcome the shortcomings of $CuFe_2O_4$, some approaches have been attempted to prepare graphene/$CuFe_2O_4$ hybrid electrodes by the hydrothermal method.[20,39] The preparation of graphene/$CuFe_2O_4$ hybrid materials as a high performance supercapacitor is highly desirable, and there are few reports on the formation mechanism of the hybrid materials. In this work, we showed graphene nanosheets decorated with $CuFe_2O_4$ nanoparticles ($CuFe_2O_4$-GN) that integrate both the electrically conductive property of graphene and the high capacitance of $CuFe_2O_4$. The strategy for the composite formation was a simple one-step reaction that included the reduction of graphene oxide (GO) to graphene and the in situ formation of $CuFe_2O_4$ on GN. The growth process of $CuFe_2O_4$ on GN was investigated by changing various experimental parameters, which showed the formation mechanism of the product. Furthermore, the $CuFe_2O_4$-GN composites possessed good electrical capacitance, which holds great promise for a wide range of electrochemical fields.

2. EXPERIMENTAL SECTION

2.1. Reagents. $CuCl_2·2H_2O$, $FeCl_3·6H_2O$, sodium acetate (NaAc), polyvinylpyrrolidone (PVP), ethylene glycol, and graphite (<20 μm) were purchased from Sigma-Aldrich. All chemicals were of analytic grade and used as received without further purification. Deionized water was filtered by using a water-purification system (UP90 model, Seoul, South Korea). Graphene oxide (GO) and graphene (GN) were prepared from graphite powder by an improved Hummers method.[40,41]

2.2. Apparatus. Sample morphologies were characterized by carrying out field emission scanning electron microscopy (SEM, Hitachi S-4800). A Transmission electron microscopy (TEM) instrument equipped with a field emission gun and operated at 200 kV was used for high-resolution TEM measurements (JEOL, JEM-2010). In thermogravimetric analysis (TGA) measurements, an analyzer (TA Instruments, Q-5000 IR) was used with a heating rate of 5 °C·min^{-1} in air. The powder X-ray diffraction spectra (XRD) were measured by X-ray diffraction (XRD, Bruker, D8-Advance) with Cu Kα radiation, λ = 1.542 Å. X-ray photoelectron spectroscopy (XPS) experiments were performed by a Sigma Probe (KRATOS, AXIS-HSi) with a monochromatic Al Kα (1486.6 eV) X-ray source at a constant power of 100 W (15 kV and 10 mA) and beam diameter of 400 μm. The magnetic properties were measured using a physical property measurement system (Quantum Design, PPMS-14). N_2 adsorption/desorption isotherms were determined by using a physisorption analyzer (Micromeritics, ASAP2020M). Electrochemical tests were performed on an electrochemical workstation (CH Instruments, 660E), and the electrolyte used was 3 M aqueous KOH solution.

2.3. Preparation of $CuFe_2O_4$ Nanosphere and $CuFe_2O_4$-GN Composite. $CuFe_2O_4$ nanospheres were obtained by a modified method similar to a previous report.[25] A mixture of 0.01 mol $CuCl_2·2H_2O$, 0.02 mol $FeCl_3·6H_2O$, 0.2 g of NaAc, and 0.1 g of PVP was dissolved into 10 mL of ethylene glycol by stirring at room temperature. The mixture was added in a Teflon-lined autoclave (20 mL) at 180 °C for 20 h. Then the solid precipitates were washed with 50 mL of water three times to remove residual ions and PVP. Finally, the product was dried in a vacuum at 60 °C for 24 h.

A $CuFe_2O_4$-GN composite was successfully fabricated through the solvothermal method. The optimized preparation was as follows: 0.01 mol $CuCl_2·2H_2O$, 0.02 mol $FeCl_3·6H_2O$, 0.01 g of GO, 0.2 g of NaAc, and 0.5 g of PVP were dissolved into 0.01 L of ethylene glycol by stirring for 10 h. The mixture was sealed in a Teflon-lined autoclave and maintained at 180 °C for 20 h. Solid precipitates were collected by a magnet after the reaction was complete. To remove the residual metal ions and organic moiety, we washed the products several times using deionized water and ethanol. Finally, the product was dried in vacuum at 60 °C for 24 h.

Important parameters, including the concentration of NaAc, GO, PVP, $CuCl_2$, and $FeCl_3$, were altered in a series of parallel experiments in order to study the formation mechanism of $CuFe_2O_4$ nanoparticles attached on GNs.

2.4. Electrochemical Testing. Before electrochemical testing, an electrode was fabricated by mixing 70 wt % of active materials with 15 wt % acetylene black, 15 wt % polyvinylidene difluoride in *N*-methyl-2-pyrrolidinone. The weight of active materials was 3 mg. Then, the slurry was coated on a pretreated battery-grade polished Ni foil (area of coating: 1 cm^2, and foil thickness: 0.2 mm) for electrical conductivity and vacuum-dried at 60 °C for 24 h. A three-electrode cell was fabricated by employing a Hg/HgO electrode as the reference electrode, the as-prepared electrode as the working electrode, and a platinum wire electrode as the counter electrode. Cyclic voltammetry (CV) and charge−discharge were measured at various scan rates and current densities, respectively

3. RESULTS AND DISCUSSION

3.1. Characterization of $CuFe_2O_4$-GN Composite. One-step synthesis under a solvothermal condition was used to fabricate the $CuFe_2O_4$-GN composite with the reaction of GO, $CuCl_2·H_2O$, $FeCl_3·H_2O$, and NaAc in the presence of PVP.

Figure 1 shows the XRD profile of the $CuFe_2O_4$-GN composite. The position and relative intensity of diffraction peaks matched well with standard XRD data for $CuFe_2O_4$ (JCPDS 01-077-0010), and no peaks of copper oxides (CuO or CuO_2) were observed. The peaks at 2θ = 30.0, 35.5, 37.0, 43.4, 46.4, 50.8, 57.3, 62.6, and 74.2° were ascribed to the (220), (311), (222), (400), (331), (422), (511), (440), and (533) crystal planes of $CuFe_2O_4$ with cubic spinel structure. These presence of these XRD peaks confirmed that $CuFe_2O_4$ was formed on GN by the solvothermal method. The relatively high diffraction peak intensities showed the highly crystalline structure of $CuFe_2O_4$. Moreover, a broad diffraction peak appeared around 23°, corresponding to the C(002) reflection,

DOI: 10.1021/am507014w
ACS Appl. Mater. Interfaces 2015, 7, 2404−2414

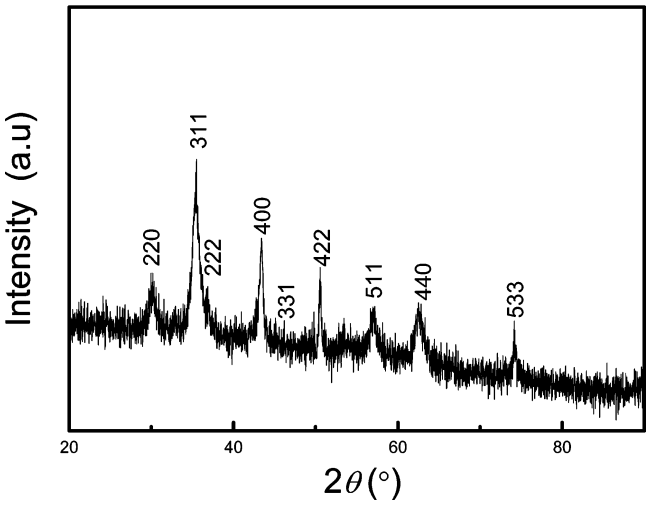

Figure 1. XRD pattern of $CuFe_2O_4$-GN composite.

which originated from GN and indicated the reduction of GO in the reaction process.[42,43]

The morphology of the typical $CuFe_2O_4$-GN composite was characterized by TEM. In Figure 2a,b, it is clearly observed that

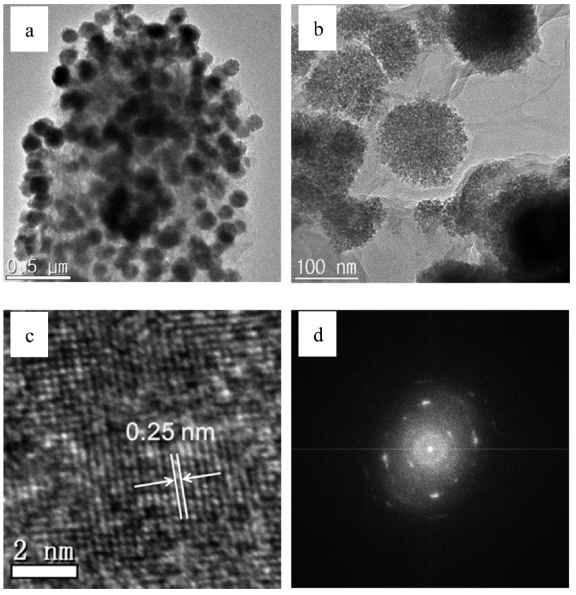

Figure 2. (a, b) TEM images of $CuFe_2O_4$-GN composite with different magnifications. (c) Lattice-resolved HRTEM image of $CuFe_2O_4$-GN composite. (d) Selected area electron diffraction pattern of $CuFe_2O_4$ in the composite.

narrowly distributed $CuFe_2O_4$ nanoparticles densely cover the surfaces of GN and exhibit a sphere-like structure with a 100 nm average size. No large aggregations of $CuFe_2O_4$ or large vacancies in GN were observed. An HRTEM image was used to further understand the dimensionality of the GN-nanoparticle morphologies. Figure 2c displays a lattice resolved HRTEM image of $CuFe_2O_4$ nanocrystal on GN. The lattice fringe spacing (0.25 nm) observed agreed well with the spacing of the (311) crystal planes of the $CuFe_2O_4$ cubic spinel structure.[20] In addition, the selected area electron diffraction (SAED) pattern in Figure 2d shows diffraction rings of the prepared $CuFe_2O_4$ nanoparticle on GN. The rings were attributed to the cubic spinel $CuFe_2O_4$ crystal structure. The TEM image of $CuFe_2O_4$ without GN is presented in the Supporting Information, Figure S1. These results were similar to our previous study.[25] The content of graphene in $CuFe_2O_4$-GN was calculated as 29 wt % by TG measurement, which is shown in the Supporting Information, Figure S2. Generally, a one-step simultaneous reduction of GO and the coating nanoparticles was the best way to achieve a GN-nanoparticle composite. This method prevented GN aggregation during the reduction process from GO, and easily obtained well-dispersed GN-nanoparticle composite easily. Furthermore, the one-step synthesis was advantageous for cost-effective production of nanomaterials. Therefore, we designed a one-step reaction to fabricate $CuFe_2O_4$-GN composites via a solvothermal process.

XPS is one of best means of further investigating the chemical composition and electronic structure of the $CuFe_2O_4$-GN. The wide scan and deconvoluted XPS spectra of the $CuFe_2O_4$-GN composite are shown in Figure 3a–d. In Figure 3a, the elements Cu, Fe, C, and O were observed clearly. Figure 3b shows the C 1s XPS spectrum of $CuFe_2O_4$-GN. The strong C 1s peak associated with C–C (284.5 eV) bonding was assigned to the graphitic carbon of GN. The other weaker peaks in Figure 3b were related to the oxygenated carbons, indicating the deoxygenation process accompanying the reduction of GO. Among the oxygen-containing groups of GN, the epoxy groups were greatly reduced in the composite. This result proved that GO could be reduced to GN with a small amount of residual oxygen-containing groups, which was why ethylene glycol was used as a reducing agent in the solvothermal reaction.[19,44]

The binding energy values of Cu 2p and Fe 2p observed in the high-resolution XPS spectra in Figure 3c,d implied that both iron and copper ions were present in the $CuFe_2O_4$-GN composite. The results were in good agreement with published work on $CuFe_2O_4$ nanoparticles.[25] Figure 3c shows that the binding energy of Cu $2p_{3/2}$ and Cu $2p_{1/2}$ at 931.9 and 951.8 eV, with a typical satellite peak of Cu^{2+} at 943.5 eV. These results suggested the presence of Cu^{2+} in $CuFe_2O_4$-GN, which was conformable with the results reported elsewhere.[20] In Figure 3d, the Fe 2p spectra showed two main peaks with binding energies of 710.2 and 724.2 eV, which were assigned to Fe $2p_{3/2}$ and Fe $2p_{1/2}$, respectively. The accompanying satellite peaks visible at binding energies of around 718.4 eV were indicative of the presence of Fe^{3+} cations. These results further confirmed the formation of $CuFe_2O_4$ in the nanocomposite.

The magnetic property of $CuFe_2O_4$-GN is shown in Figure S3 (Supporting Information). The sample presented a typical hysteresis loop in the field range of ±1500 Oe, indicating that the composite exhibited the behavior of soft magnetic semiconductor material at room temperature. The saturation magnetization, remanent magnetization, and coercivity values of $CuFe_2O_4$-GN were 30.0 emu·g^{-1}, 3.5 emu·g^{-1}, and 26.5 Oe, respectively. However, the saturation magnetization of $CuFe_2O_4$-GN was higher than that reported for $CuFe_2O_4$ (22.2 emu·g^{-1}).[20] The reason for the higher saturation magnetization might be associated with the fine nanostructure of $CuFe_2O_4$ nanoparticles on GN. It should be pointed out that an external magnet could be easily separate the $CuFe_2O_4$-GN.

The Brunauer–Emmett–Teller (BET) specific surface area of $CuFe_2O_4$-GN and $CuFe_2O_4$ were evaluated by nitrogen isothermal adsorption (in Figure S4, Supporting Information). The composites had a higher specific surface area (35 m^2·g^{-1}) than that of $CuFe_2O_4$ (22 m^2·g^{-1}).

3.2. Formation Mechanism of $CuFe_2O_4$-GN Composite. During the preparation of metal oxide nanostructures

DOI: 10.1021/am507014w
ACS Appl. Mater. Interfaces 2015, 7, 2404–2414

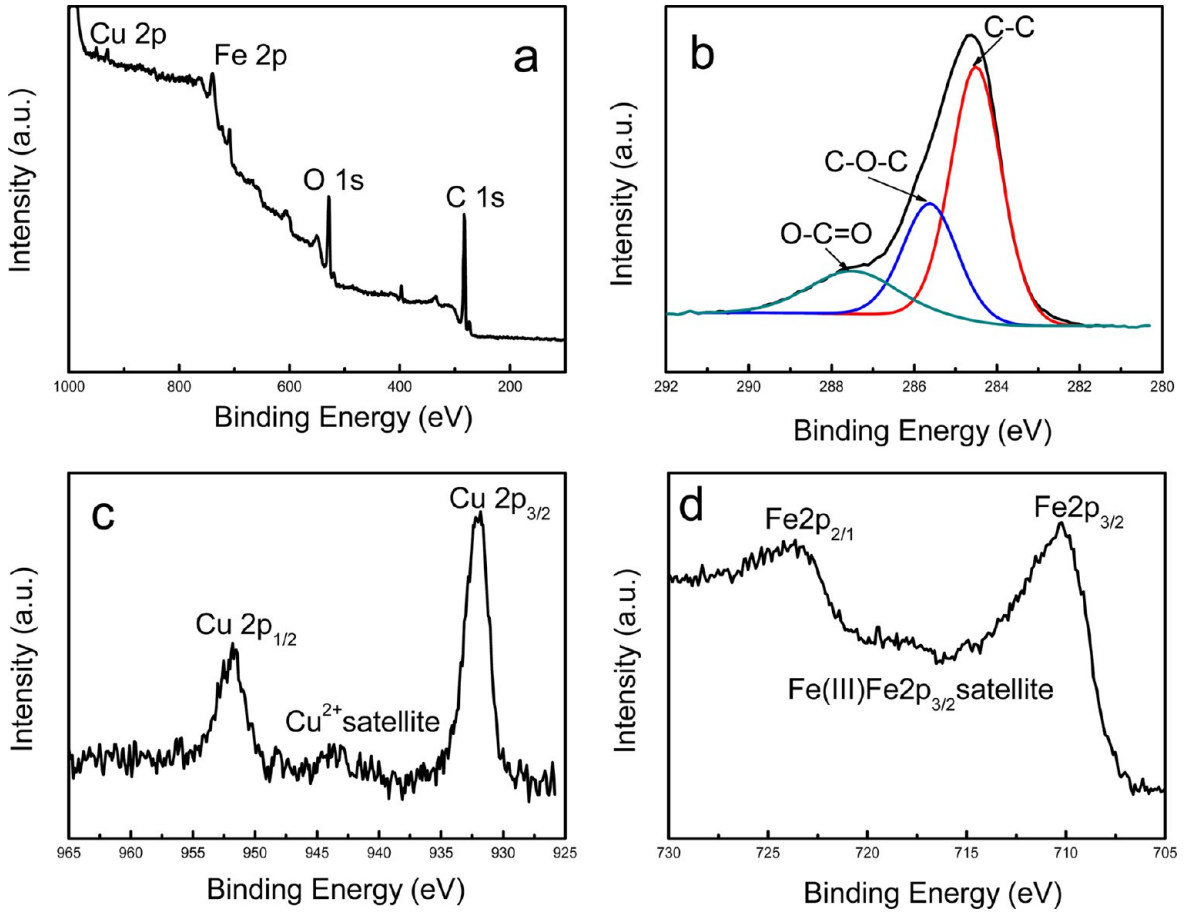

Figure 3. (a) Wide scan and (b–d) deconvoluted XPS spectra of $CuFe_2O_4$-GN.

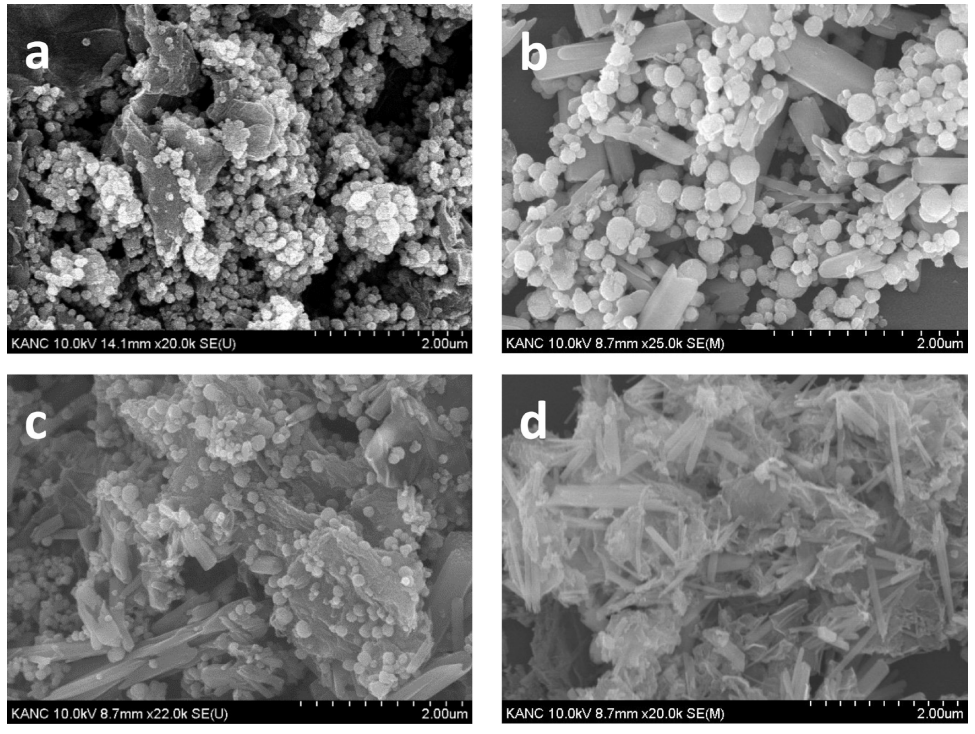

Figure 4. SEM images of $CuFe_2O_4$-GN at different GO concentrations ($g \cdot L^{-1}$): (a) 0.5, (b) 1.0, (c) 2.0, and (d) 4.0. Other conditions: 2 $mol \cdot L^{-1}$ $FeCl_3$, 1 $mol \cdot L^{-1}$ $CuCl_2$, 10 $g \cdot L^{-1}$ NaAc, 50 $g \cdot L^{-1}$ PVP, 180 °C, 20 h.

DOI: 10.1021/am507014w
ACS Appl. Mater. Interfaces 2015, 7, 2404–2414

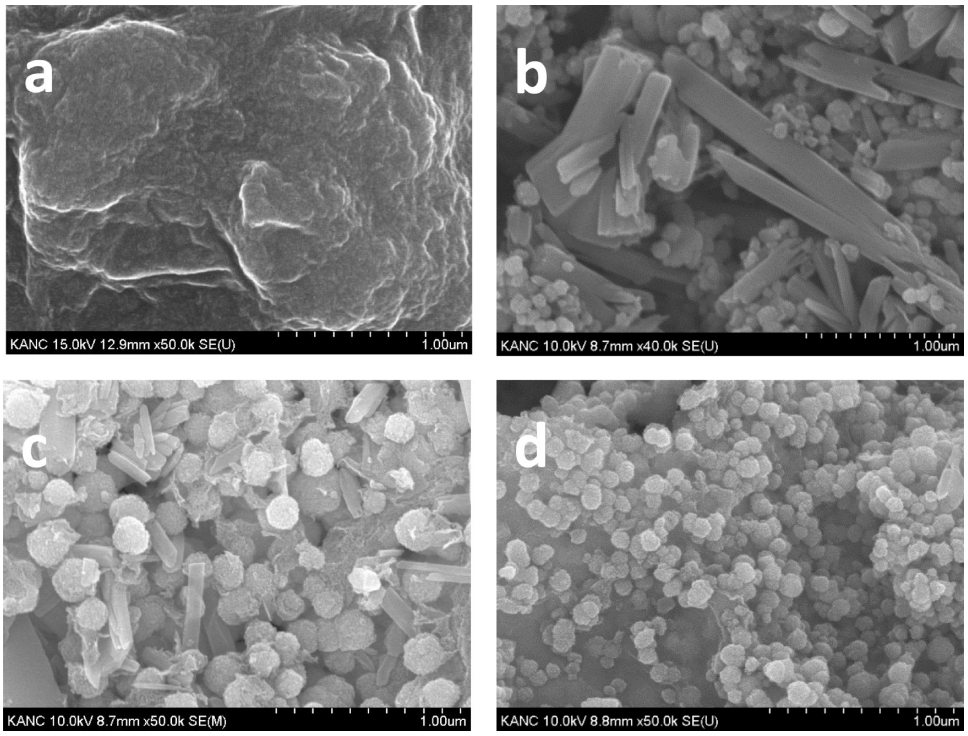

Figure 5. SEM images of $CuFe_2O_4$-GN at different NaAc concentration ($g \cdot L^{-1}$): (a) 0, (b) 10, (c) 15, and (d) 20. Other conditions: 2 $mol \cdot L^{-1}$ $FeCl_3$, 1 $mol \cdot L^{-1}$ $CuCl_2$, 1 $g \cdot L^{-1}$ GO, 50 $g \cdot L^{-1}$ PVP, 180 °C, 20 h.

from the solvothermal method, we found that the preparation conditions had an important influence on the quality of the obtained nanomaterial. For that reason, the potential influencing factors in the process were studied to understand the mechanism of formation of $CuFe_2O_4$ nanoparticles on GN.

3.2.1. Effect of GO Concentration. To investigate the effect of the amount of GO on the morphology of $CuFe_2O_4$ nanostructures, a number of experiments were carried out by changing the amount of GO, when other conditions were fixed. The SEM results are shown in Figure 4a–d. When 0.5 $g \cdot L^{-1}$ GO was in the initial solution, the $CuFe_2O_4$ sample exhibited uniform nanoparticles with an average diameter of 90 nm. There were few GNs owing to the low concentration of GO. When more GO (1.0 and 2.0 $g \cdot L^{-1}$) was added to the initial solution, nanorods were observed, as shown in Figure 4b,c. Furthermore, when the concentration of GO reached 4.0 $g \cdot L^{-1}$, the $CuFe_2O_4$ nanoparticles were hardly observable (Figure 4d). By contrast, many smaller nanorods were modified on GN than those in Figure 4b,c. To investigate the structure of the nanorods in Figure 4d, an XRD experiment was conducted, as shown in Figure S5 (Supporting Information). The peaks located at 43.3, 50.5, and 74.0° were assigned to the (110), (200), and (220) crystal planes of Cu, respectively, which were consistent with the standard reported values (JCPDS File no. 04-0836). These XRD results demonstrated the formation of Cu nanorods on GN instead of $CuFe_2O_4$.

These results, based on the addition of GO, suggestted that GO strongly affected the formation of $CuFe_2O_4$ and Cu nanomaterials. As the GO concentration increased, it was easy to generate Cu nanorods instead of $CuFe_2O_4$ nanoparticles. Usually, the absence of GO in the Cu/Fe system would yield irregular copper, because some of Cu^{2+} was reduced to copper metal by ethylene glycol.[18,45,46] It was known that GO was a type of carbon nanomaterial covered with hydroxyl groups on the hexagonal basal plane[47] and could serve as a mild reducing agent, which confirmed that it was the key to the formation of Cu nanorods in a NaOH environment.[48] Therefore, the synergistic effect between GO and ethylene glycol promoted the growth of Cu nanorods, and NaAc, acting as the precipitation agent, was consumed resulting in the decline of $CuFe_2O_4$ nanoparticle formation on GN. Thus, the concentration of GO should be controlled during preparation of $CuFe_2O_4$-GN composites.

3.2.2. Effect of NaAc Concentration. NaAc was widely used as a precipitation agent in the preparation of metal oxide nanomaterials.[49,50] Figure 5 shows $CuFe_2O_4$-GN composite prepared with a mixture of 2 $mol \cdot L^{-1}$ $FeCl_3$, 1 $mol \cdot L^{-1}$ $CuCl_2$, 1 $g \cdot L^{-1}$ GO, and 50 $g \cdot L^{-1}$ PVP at 180 °C for 20 h with different amount of NaAc (0, 10, 15, 20 $g \cdot L^{-1}$). When no NaAc was added, no particles formed on GN. As the concentration of NaAc was added, the composite was mainly composed of Cu nanorods on GN, as shown in Figure 5b; however, $CuFe_2O_4$ small nanoparticles (90 nm) began to form. In Figure 5c, the amount of $CuFe_2O_4$ nanoparticles increased with the decrease of Cu nanorods. Moreover, the size of $CuFe_2O_4$ nanoparticles was larger than that prepared by 10 $g \cdot L^{-1}$ NaAc. When the concentration of NaAc was further increased to 20 $g \cdot L^{-1}$, uniform $CuFe_2O_4$ nanoparticles formed on GN without Cu nanorods, as see in Figure 5d. These results showed that NaAc was necessary for the formation of $CuFe_2O_4$ nanoparticles in the system.

The effect of the amount of NaAc on the morphology of the nanoparticles could be explained by the formation of metal oxides in the solvothermal system. Typically, the formation of metal oxide nanoparticles on GNs by the solvothermal method involves three steps including the nucleation, growth, and assembly of nanocrystals. The morphology of nanomaterials was also strongly dependent on the pH of the solution system.

DOI: 10.1021/am507014w
ACS Appl. Mater. Interfaces 2015, 7, 2404–2414

In the preparation of $CuFe_2O_4$-GN, the three steps might occur simultaneously. When the amount of NaAc was low, the nucleation step for the formation of $CuFe_2O_4$ could be prevented while instead of Cu nanorods, indicating that the nucleation rate of a $CuFe_2O_4$ nanocrystal was slower than that of Cu. Meanwhile, the self-assembly step for the Cu nanocrystal had no limitation to form the Cu nanorod while consuming NaAc. Under higher concentrations of NaAc, the nucleation rate of $CuFe_2O_4$ nanocrystal might be faster than that of Cu, because NaAc could act as a mineralizer between Fe and Cu precursors and increase the chemical potential of the solution. This leads to a dissolution−recrystallization process of $CuFe_2O_4$ into the stable phase,[25] by contrast, a lack of Cu nanocrystals ressulted in preventing the formation of Cu nanorod on GN.

In addition to the SEM investigation, the evolution of $CuFe_2O_4$-GN crystal structure was studied. Figure 6 shows the

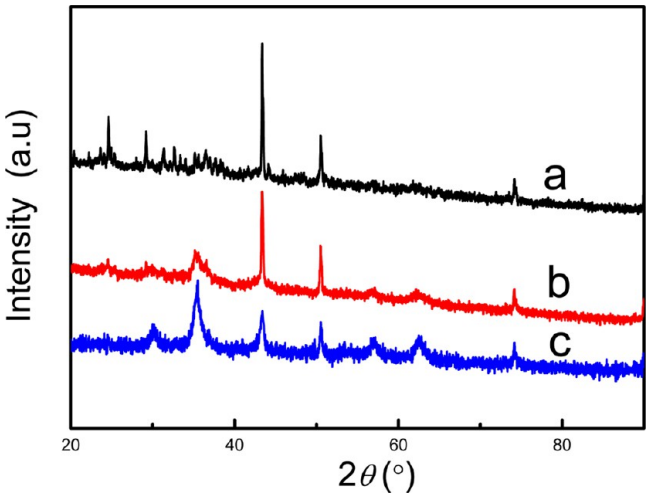

Figure 6. XRD patterns of $CuFe_2O_4$-GN composite prepared at different NaAc concentrations ($g \cdot L^{-1}$): (a) 10, (b) 15, and (c) 20. Other conditions: 2 $mol \cdot L^{-1}$ $FeCl_3$, 1 $mol \cdot L^{-1}$ $CuCl_2$, 1 $g \cdot L^{-1}$ GO, 50 $g \cdot L^{-1}$ PVP, 180 °C, 20 h.

XRD patterns of the products prepared by different NaAc concentrations. When 10 $mg \cdot mL^{-1}$ NaAc was added, several broad peaks from 20° to 40° were observed in the XRD patterns, indicating that the precursors began to transform into amorphous $CuFe_2O_4$ at the low NaAc concentration. In Figure 6b, new diffraction peaks associated with planes of (220), (400), (107), (422), (511), (440), and (533) appeared. The intensity of the peak corresponding to the (311) crystal planes of $CuFe_2O_4$ increased remarkably, suggesting that the growth of $CuFe_2O_4$ nanoparticles on GN was oriented with (311) crystal plane. When the concentration of NaAc was increased to 20 $mg \cdot mL^{-1}$, the intensities of the diffraction peaks of $CuFe_2O_4$ further increased, indicating enhanced crystallinity. Moreover, no diffraction peak was attributed to iron oxide or copper oxide, which proved that pure $CuFe_2O_4$ was prepared at a high concentration of NaAc.

3.2.3. Effect of Precursor Concentration. In the process of preparing $CuFe_2O_4$-GN, the initial concentration of the precursor was one of the most important factors because it could affect formation of $CuFe_2O_4$ nanoparticles including the nucleation, growth of the primary crystal, and self-assembly of the nanoparticle. Figure 7 shows the SEM images of the $CuFe_2O_4$-GN composite under different initial precursor concentrations between $FeCl_3$ and $CuCl_2$. At a low concentration of precursor, only a few irregular $CuFe_2O_4$ nanoparticles began to grow on the surface of GN. When a higher concentration of precursor was added, a more regular morphology of porous $CuFe_2O_4$ formed on GN. The diameter of $CuFe_2O_4$ nanoparticles increased with the increase of the precursor concentration. In Figure 7d, when the concentrations of $FeCl_3$ and $CuCl_2$ were 6 and 3 $mol \cdot L^{-1}$, uniform and regular $CuFe_2O_4$ nanoparticles (∼150 nm) were obtained in the $CuFe_2O_4$-GN composite. These results showed that the concentration of Fe/Cu precursors was a determining factor that affected the regularity and the morphology of the $CuFe_2O_4$-GN composite, following the theory of Von Weimarn.[51] At a low Fe/Cu precursor concentration, although the rates of both nucleation and growth were slow, the precursors could nucleate because there was enough precipitation agent, which resulted in a lack of precursors for the self-assembly step, and thus uniform $CuFe_2O_4$ nanoparticle were hardly generated on GN. When the concentration of the precursors increased, the rate of nucleation could not sustain an increase due to the limitation of the precipitation agent. However, the growth and self-assembly steps were ongoing, so $CuFe_2O_4$ nanoparticles became large. Therefore, keeping a defined concentration of GO and precipitation agent, the size of the $CuFe_2O_4$ nanoparticles on GN was completely dependent on the precursor concentration.

3.2.4. Effect of the Stabilization Agent. The effect of the stabilization agent PVP on the morphology of $CuFe_2O_4$-GN was also studied. SEM images of $CuFe_2O_4$-GN prepared with different amounts of PVP at 180 °C for 20 h are shown in Figure 8. When no PVP was used, $CuFe_2O_4$ nanoparticles were generated on GN with uniform size (∼150 nm), which differed from $CuFe_2O_4$ without GN. This indicated that GN might adopt particular crystallographic facets of the growing crystal as well as some capping agents. With the increase of PVP, the size of the $CuFe_2O_4$ nanoparticles decreased. If the PVP concentration was increased, it could adsorb on the crystals of $CuFe_2O_4$, which would prevent the aggregation of $CuFe_2O_4$ for either a stereo-barrier or an electrostatic repulsive interaction,[52,53] leading to small nanospheres. In Figure 8d, $CuFe_2O_4$ nanoparticles were smaller, and their size distribution widened. It was suggested that high concentrations of PVP provided a strong capping effect, which impeded the growth of $CuFe_2O_4$. Moreover, PVP as a surfactant in high concentrations could self-assemble to form micelles or reverse micelles, which could weaken the size-control effect.

3.3. Electrochemical Tests. It was well-known that metal oxide−carbon nanomaterials have been found to be remarkably advantageous as supercapacitors because carbon nanomaterials, such as carbon nanotube and graphene, provided a high surface area and conductivity leading to the deposition of nanostructured metal oxides with high specific capacitance.[54] Recently, it was reported that $CuFe_2O_4$ nanomaterials possessed good electrochemical properties. However, studies of $CuFe_2O_4$ on GN have revealed little about high performance supercapacitors. In this work, the electrochemical performance of $CuFe_2O_4$-GN composites was investigated by CV and galvanostatic charge/discharge measurements.

Figure 9 illustrates the CV curves of the as-prepared $CuFe_2O_4$-GN and $CuFe_2O_4$ composites from −0.2 to +0.7 V vs Hg/HgO at a scan rate of 50 $mV \cdot s^{-1}$. A pair of well redox peaks in the CV curves appeared for $CuFe_2O_4$-GN was clearly found as well as that of $CuFe_2O_4$, indicating the fast redox

DOI: 10.1021/am507014w
ACS Appl. Mater. Interfaces 2015, 7, 2404−2414

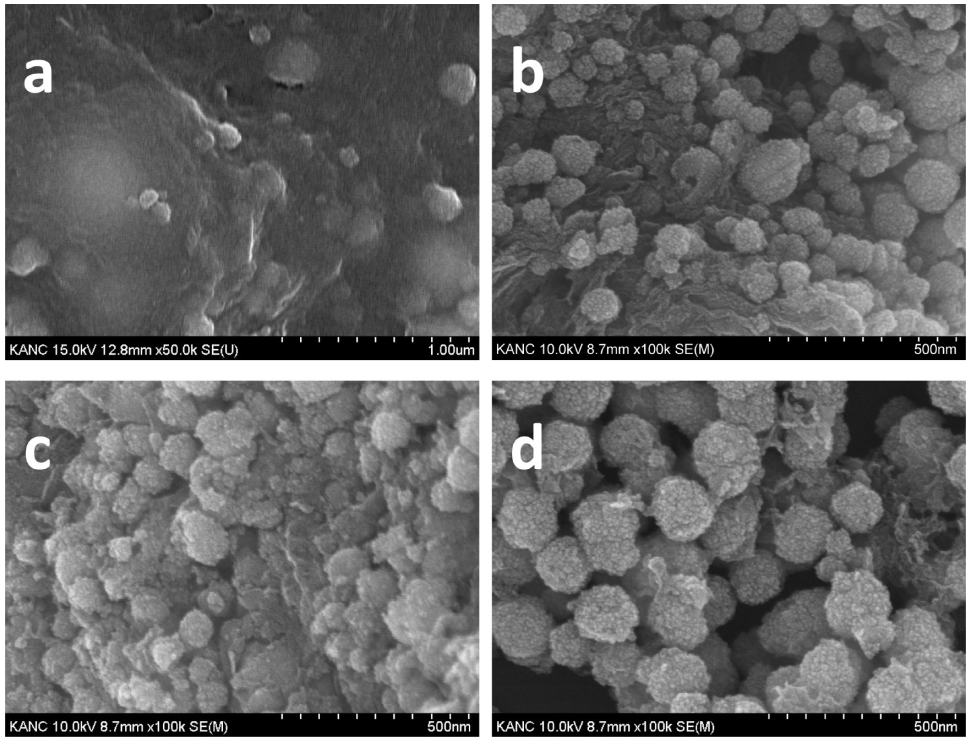

Figure 7. SEM images of $CuFe_2O_4$-GN at different precursor concentrations ($FeCl_3$ and $CuCl_2$, mol·L^{-1}): (a) 1, 0.5, (b) 2, 1 (c) 4, 2, and (d) 6, 3. Other conditions: 20 g·L^{-1} NaAc, 1 g·L^{-1} GO, 50 g·L^{-1} PVP, 180 °C, 20 h.

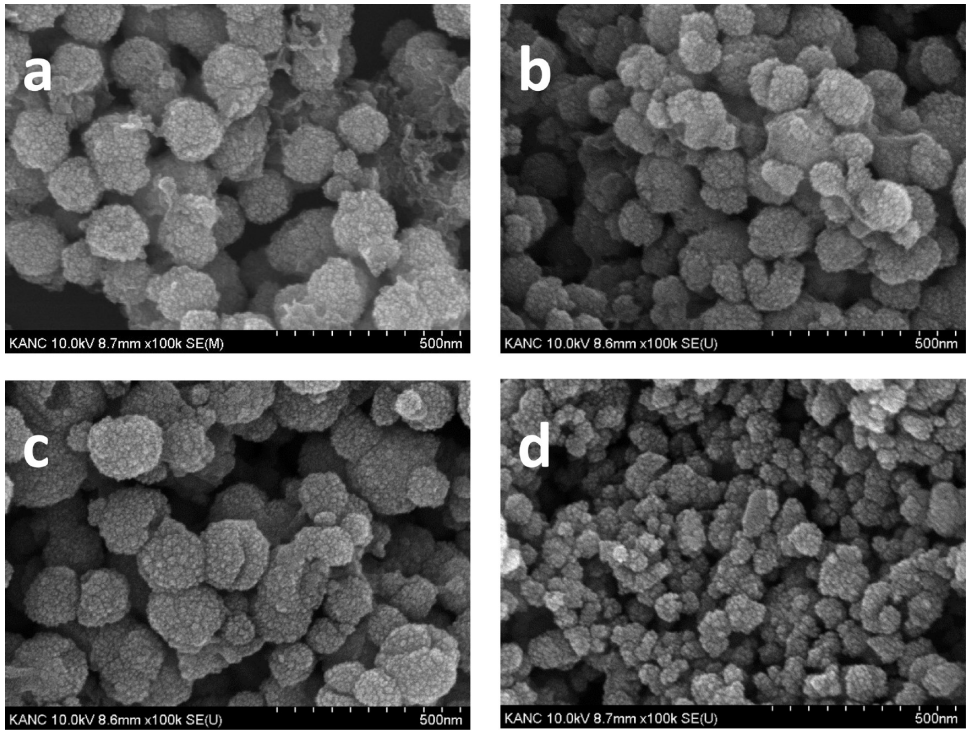

Figure 8. SEM images of $CuFe_2O_4$-GN at different PVP concentrations (g·L^{-1}): (a) 0, (b) 50, (c) 100, and (d) 150. Other conditions: 2 mol·L^{-1} $FeCl_3$, 1 mol·L^{-1} $CuCl_2$, 20 g·L^{-1} NaAc, 1 g·L^{-1} GO, 180 °C, 20 h.

reaction of $CuFe_2O_4$ in the composites. Therefore, the capacitances of $CuFe_2O_4$-GN mainly originated from pseudocapacitance. Compared with $CuFe_2O_4$, the higher response of the peak current of $CuFe_2O_4$-GN meant higher specific capacitance. Moreover, the redox potential peaks of $CuFe_2O_4$-GN shifted negatively due to the excellent conductivity of GN.

To evaluate the relationship between the scan rate and supercapacitive performance of $CuFe_2O_4$-GN, the CV studies were performed at different scan rates (10−100 mV·s^{-1}) in 3 M KOH. In Figure 10a, the redox process at different scan rates showed that the peak potential and current were affected by scan rate. The obvious increase of current peaks by scan rate

DOI: 10.1021/am507014w
ACS Appl. Mater. Interfaces 2015, 7, 2404−2414

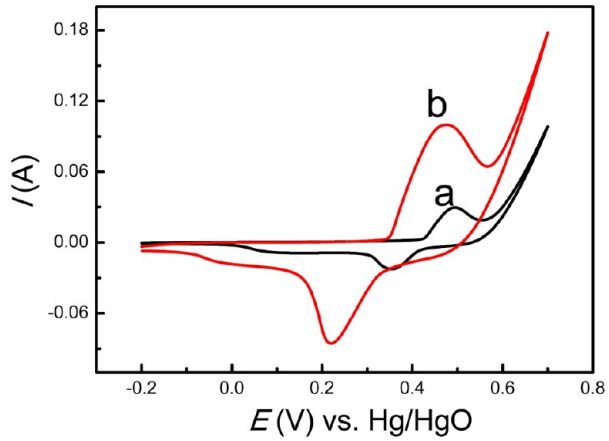

Figure 9. At 25 °C, scan rate 50 mV s^{-1}, CV curves of the electrodes of $CuFe_2O_4$ (a) and $CuFe_2O_4$-GN (b) in 3 M KOH.

indicated a good rate capability of the composites.[55] Furthermore, the peak current showed a well linear relationship to the square root of the scanning rate in Figure 10b, suggesting that the electrochemical process of $CuFe_2O_4$-GN occurring on the electrode surface was a diffusion-controlled process.

The specific capacitance of $CuFe_2O_4$-GN with increasing discharge current density (1.0, 1.5, 2.0, 2.5, and 3.0 A·g^{-1}) is shown in Figure 11. The experimental results showed that the galvanostatic discharge time for $CuFe_2O_4$-GN was significantly greater than $CuFe_2O_4$ and GN (Figures S6 and S7, Supporting Information). This data assuredly suggested that $CuFe_2O_4$-GN had the larger charge capacity, which was consistent with the CV results. The specific capacitance of the composite could be calculated by the following equation:[50]

$$C_S = i\Delta t/(m\Delta E)$$

Where i (A) referred to the charge (or discharge) current, Δt (s) was the discharge time, m (g) represented the mass of supercapacitive material, and ΔE (V) was the potential window.

The relation between the specific capacitance and current density was plotted as in Figure 12b. It was noted that the largest specific capacitance could be reached up to 576.6 F·g^{-1} when the current density was 1 A·g^{-1}. For the same sample, decreasing the discharge current density resulted in higher specific capacitances, because the diffusing rate of electrolyte anions into the electrode increased with the decreasing current

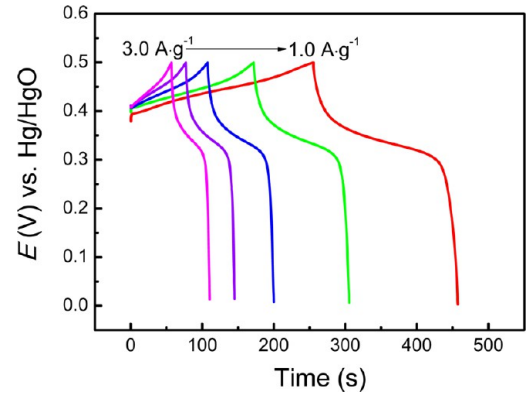

Figure 11. Charge−discharge curves of $CuFe_2O_4$-GN electrode at different current densities.

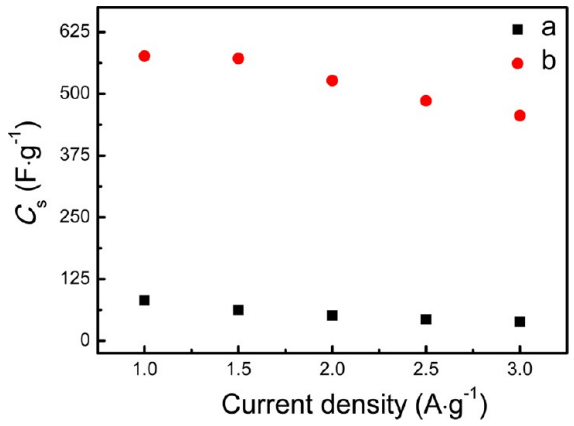

Figure 12. Relationship between the specific capacitance and the current density: (a) $CuFe_2O_4$, (b) $CuFe_2O_4$-GN.

density, leading to enhance the capacitance. The composite kept 79.1% of its capacitance (576.6−456.0 F·g^{-1}) as current density was increased from 1.0 to 3.0 A·g^{-1}, whereas $CuFe_2O_4$ lost 48.2% (81.5−39.3 F·g^{-1}) of its capacitance in the same conditions. The results showed a greatly improved capacitance of $CuFe_2O_4$-GN and enhanced rate capability compared to $CuFe_2O_4$.

Although the theoretical capacitance of a single-layer GN was 550 F·g^{-1},[56] currently, the specific capacitances of GN was

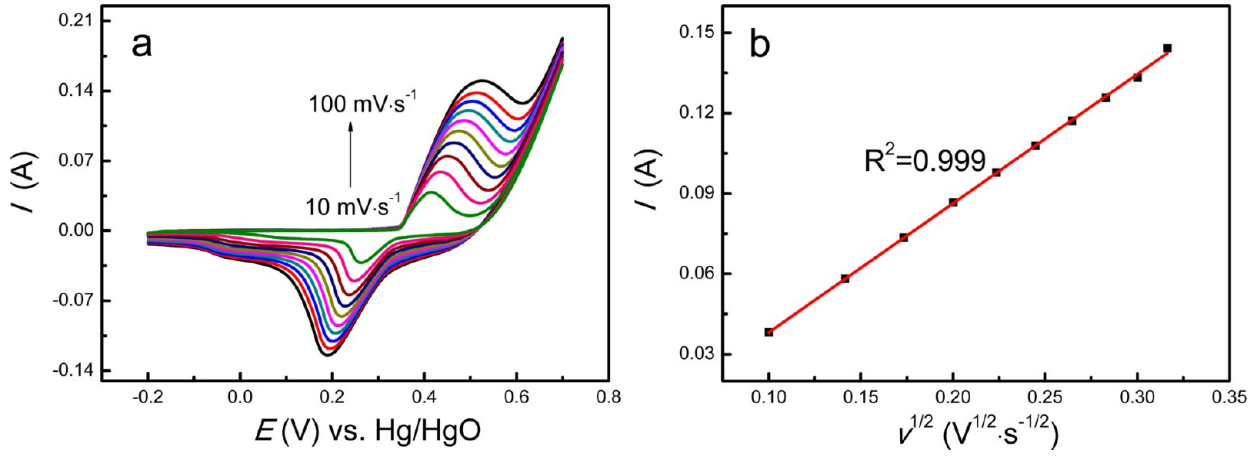

Figure 10. (a) At 25 °C, CV curves of the $CuFe_2O_4$-GN electrode in 3 M KOH with various scan rates. (b) Plot of i and $v^{1/2}$.

DOI: 10.1021/am507014w
ACS Appl. Mater. Interfaces 2015, 7, 2404−2414

Table 1. Comparison of the Specific Capacitance of Some Related Materials in the Literature

sample	specific capacitance ($F \cdot g^{-1}$)	potential range (V)	electrolyte	mass (mg)	current density	reference
$CuFe_2O_4$-GN	576.6	0−0.5	3 M KOH	3	1.0 $A \cdot g^{-1}$	our work
$CuFe_2O_4$ film	5.7	−0.2−+0.7	1 M NaOH		0.3 $\mu A \cdot cm^{-2}$	60
$CuFe_2O_4$ fiber	28	−0.1−+0.4	1 M KOH	5	0.5 $A \cdot g^{-1}$	24
$CuFe_2O_4$ nanowires/CNT	267	−0.3−+1.0	1 M KCl	0.12		61
$CuFe_2O_4$ nanosphere	334	0−0.4	1 M KOH	3	0.6 $A \cdot g^{-1}$	25

61.7−22.3 $F \cdot g^{-1}$ as current density was increased from 1.0 to 3.0 $A \cdot g^{-1}$ in Figure S8 (Supporting Information). It was similar to other GN-based supercapacitors in many reports[57−59] due to the GN aggregation of $\pi-\pi$ interaction. In Figure S9 (Supporting Information), the SEM image of GN clearly shows that the GN, as the aggregation form, was instead of a GN single layer. The aggregation was unavoidable and dramatically degraded the specific capacitances due to intense $\pi-\pi$ interaction. However, in this solvothermal method, Fe^{3+} and Cu^{2+} ions were coordinated to the surfaces of GO and then transformed into $CuFe_2O_4$, giving rise to $CuFe_2O_4$-GN hybrid nanosheets. The uniform dispersion of $CuFe_2O_4$ NP growing on the GN surfaces could weaken the effect of GN $\pi-\pi$ interaction, thus avoiding the aggregation of graphene. Therefore, the result of $CuFe_2O_4$-GN showed much better electrochemical capacity.

The specific capacitance values of $CuFe_2O_4$ materials are presented in Table 1. It was found that $CuFe_2O_4$-GN had a high capacitance compared to $CuFe_2O_4$ and other related materials.[24,25,60,61] To evaluate the key parameters of the supercapacitor, the energy density (E) and power density (P) were calculated from galvanostatic charge/discharge curves by the following equations:[62]

$$E = \frac{1}{2} C \Delta V^2$$

$$P = E/\Delta t$$

where E is the average energy density ($W \cdot h \cdot kg^{-1}$), C is the specific capacitance based on the mass of the electroactive material ($F \cdot g^{-1}$), V is the potential window of discharge (V), P is the power density ($W \cdot kg^{-1}$), and Δt is the discharge time (s). In Figure S10 (Supporting Information), the Ragone plots of $CuFe_2O_4$ and $CuFe_2O_4$-GN also showed that the $CuFe_2O_4$-GN has higher power capability than $CuFe_2O_4$. The $CuFe_2O_4$-GN composite delivers a high energy density of 15.8 $W \cdot h \cdot kg^{-1}$ at a power density of 1.1 $kW \cdot kg^{-1}$, which is about 11 times larger than that of $CuFe_2O_4$.

Figure 13 displays the stability of $CuFe_2O_4$-GN and $CuFe_2O_4$ by continuous charge−discharge measurements at 1 $A \cdot g^{-1}$ for 1000 cycles. $CuFe_2O_4$-GN exhibited higher stability than $CuFe_2O_4$. After 300 cycles, the capacitance retention of the composites was 85%, while that of the pristine $CuFe_2O_4$ was only 58%, revealing that the $CuFe_2O_4$-GN electrode had good recycle properties for electrochemical capacitors. As a result, the good stability of $CuFe_2O_4$-GN arose from the synergistic effect between $CuFe_2O_4$ nanoparticles and GN. However, $CuFe_2O_4$ nanoparticles decorated on GN sheets could effectively reduce the diffusion and migration distance of the electrolyte ions during the fast electrochemical process. On the other hand, GN had high conductivity for $CuFe_2O_4$-GN composites inside the electrode, resulting in the enhanced electrochemical stability. The electrode morphology including $CuFe_2O_4$-GN, acetylene black, and PVDF before and after cyclic test was observed in Figure S11 (Supporting Information). The SEM images in Figure S11 (Supporting Information) show that the surface morphology of the composite was retained, which suggested the cyclic test hardly affect the composite nanostructure. It seemed that GN was helpful to maintain the initial structure of $CuFe_2O_4$-GN.

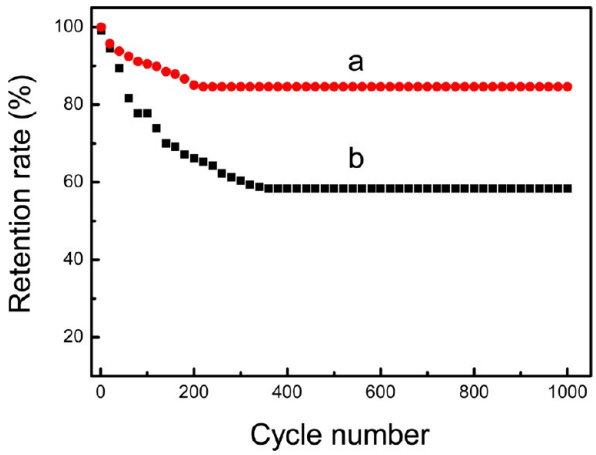

Figure 13. Cycle stability of (a) $CuFe_2O_4$-GN and (b) $CuFe_2O_4$ specific capacitance at a constant current of 1.0 $A \cdot g^{-1}$.

Although the three-electrode system test was useful to investigate the electrochemical behavior of the electrode material, obviously, for practical application of supercapacitors, the two-electrode system could get the reliable data, The electrochemical charge−discharge test at 1 $A \cdot g^{-1}$ of $CuFe_2O_4$-GN was studied in a two-electrode system, as shown in Figure S12 (Supporting Information). The specific capacitance was calculated as 125.7 $F \cdot g^{-1}$. The result was smaller than that of the three-electrode system. It will be taken into full account in future research that the two-electrode system improved the property of $CuFe_2O_4$-GN for a supercapacitor material.

4. CONCLUSIONS

In summary, we developed a facile, scalable, and cost-effective solvothermal approach to prepare multifunctional $CuFe_2O_4$-GN as a high performance supercapacitor material. Also, the possible formation mechanisms of $CuFe_2O_4$-GN were presented by investigating the effects of various experimental parameters. Graphene in the composites played a considerable role in obtaining uniform $CuFe_2O_4$ nanoparticles and enhancing the electrochemical property of $CuFe_2O_4$-GN. Because of good electrical conductivity and hierarchical structure, the composite had significantly enhanced electrochemical capacitance (576.6 $F \cdot g^{-1}$ at 1 $A \cdot g^{-1}$), rate performance, and cycling stability (85% capacitance retention after 1000 cycles) compared to pure $CuFe_2O_4$ nanoparticles. Accordingly, the results suggested that the composites are very promising candidates for supercapacitor materials.

DOI: 10.1021/am507014w
ACS Appl. Mater. Interfaces 2015, 7, 2404−2414

■ ASSOCIATED CONTENT

Supporting Information

TEM image of $CuFe_2O_4$ nanoparticles, TG curve, magnetic hysteresis curve of $CuFe_2O_4$-GN, N_2 adsorption/desorption isotherms, XRD pattern of $CuFe_2O_4$-GN, charge−discharge curves of $CuFe_2O_4$ and GN electrode at different current densities, relationship between the specific capacitance and the current density of GN, SEM image of GN, Ragone plots related to energy density and power density of the composites, SEM images of $CuFe_2O_4$-GN, and charge−discharge curves of $CuFe_2O_4$-GN electrode in two-electrode system. This material is available free of charge via the Internet at http://pubs.acs.org.

■ AUTHOR INFORMATION

Corresponding Authors

*Y. Piao. E-mail: parkat9@snu.ac.kr. Tel: +82 318889148.
*G. Diao. E-mail: gwdiao@yzu.edu.cn. Tel: +86 51487975436. Fax: +86 514 87975244.

Notes

The authors declare no competing financial interest.

■ ACKNOWLEDGMENTS

This work was supported by Nano Material Technology Development Program (2014M3A7B6020163) of MSIP/NRF and by the Center for Integrated Smart Sensors funded by the Ministry of Science, ICT and Future Planning, Republic of Korea, as Global Frontier Project (CISS-012M3A6A6054186).

■ REFERENCES

(1) Miller, J. R.; Simon, P. Materials Science. Electrochemical Capacitors for Energy Management. *Science* **2008**, *321*, 651−652.
(2) Simon, P.; Gogotsi, Y.; Dunn, B. Where Do Batteries End and Supercapacitors Begin? *Science* **2014**, *343*, 1210−1211.
(3) Naoi, K.; Naoi, W.; Aoyagi, S.; Miyamoto, J.; Kamino, T. New Generation "Nanohybrid Supercapacitor. *Acc. Chem. Res.* **2012**, *46*, 1075−1083.
(4) Deng, W.; Ji, X.; Chen, Q.; Banks, C. E. Electrochemical Capacitors Utilising Transition Metal Oxides: An Update of Recent Developments. *RSC Adv.* **2011**, *1*, 1171−1178.
(5) Wang, G.; Zhang, L.; Zhang, J. A Review of Electrode Materials for Electrochemical Supercapacitors. *Chem. Soc. Rev.* **2012**, *41*, 797−828.
(6) Zheng, J. P.; Cygan, P. J.; Jow, T. R. Hydrous Ruthenium Oxide as an Electrode Material for Electrochemical Capacitors. *J. Electrochem. Soc.* **1995**, *142*, 2699−2703.
(7) McKeown, D. A.; Hagans, P. L.; Carette, L. P. L.; Russell, A. E.; Swider, K. E.; Rolison, D. R. Structure of Hydrous Ruthenium Oxides: Implications for Charge Storage. *J. Phys. Chem. B* **1999**, *103*, 4825−4832.
(8) Simon, P.; Gogotsi, Y. Materials for Electrochemical Capacitors. *Nat. Mater.* **2008**, *7*, 845−854.
(9) Lei, Y.; Li, J.; Wang, Y.; Gu, L.; Chang, Y.; Yuan, H.; Xiao, D. Rapid Microwave-Assisted Green Synthesis of 3D Hierarchical Flower-Shaped $NiCo_2O_4$ Microsphere for High-Performance Supercapacitor. *ACS Appl. Mater. Interfaces* **2014**, *6*, 1773−1780.
(10) Zheng, F.; Zhu, D.; Chen, Q. Facile Fabrication of Porous $Ni_xCo_{3-x}O_4$ Nanosheets with Enhanced Electrochemical Performance as Anode Materials for Li-Ion Batteries. *ACS Appl. Mater. Interfaces* **2014**, *6*, 9256−9264.
(11) Ahmed, M. S.; Jeon, S. Highly Active Graphene-Supported Ni_xPd_{100-x} Binary Alloyed Catalysts for Electro-Oxidation of Ethanol in an Alkaline Media. *ACS Catal.* **2014**, *4*, 1830−1837.
(12) Yang, Y.; Fei, H.; Ruan, G.; Xiang, C.; Tour, J. M. Efficient Electrocatalytic Oxygen Evolution on Amorphous Nickel−Cobalt Binary Oxide Nanoporous Layers. *ACS Nano* **2014**, *8*, 9518−9523.
(13) Yin, Z.; Zheng, Q.; Chen, S.; Cai, D. Interface Control of Semiconducting Metal Oxide Layers for Efficient and Stable Inverted Polymer Solar Cells with Open-Circuit Voltages over 1.0 V. *ACS Appl. Mater. Interfaces* **2013**, *5*, 9015−9025.
(14) Augustyn, V.; Simon, P.; Dunn, B. Pseudocapacitive Oxide Materials for High-Rate Electrochemical Energy Storage. *Energy Environ. Sci.* **2014**, *7*, 1597−1614.
(15) Wang, S.; Ho, K.; Kuo, S.; Wu, N. Investigation on Capacitance Mechanisms of Fe_3O_4 Electrochemical Capacitors. *J. Electrochem. Soc.* **2006**, *153*, A75−A80.
(16) Kuo, S.; Wu, N. Electrochemical Characterization on $MnFe_2O_4$/Carbon Black Composite Aqueous Supercapacitors. *J. Power Sources* **2006**, *162*, 1437−1443.
(17) Yu, L.; Zhang, G.; Yuan, C.; Lou, X. W. Hierarchical $NiCo_2O_4$@MnO_2 Core-Shell Heterostructured Nanowire Arrays on Ni Foam as High-Performance Supercapacitor Electrodes. *Chem. Commun.* **2013**, *49*, 137−139.
(18) Zhang, H.; Gao, S.; Shang, N.; Wang, C.; Wang, Z. Copper Ferrite−Graphene Hybrid: A Highly Efficient Magnetic Catalyst for Chemoselective Reduction of Nitroarenes. *RSC Adv.* **2014**, *4*, 31328−31332.
(19) Zhao, Y.; He, G.; Dai, W.; Chen, H. High Catalytic Activity in the Phenol Hydroxylation of Magnetically Separable $CuFe_2O_4$−Reduced Graphene Oxide. *Ind. Eng. Chem. Res.* **2014**, *53*, 12566−12574.
(20) Fu, Y.; Chen, Q.; He, M.; Wan, Y.; Sun, X.; Xia, H.; Wang, X. Copper Ferrite-Graphene Hybrid: A Multifunctional Heteroarchitecture for Photocatalysis and Energy Storage. *Ind. Eng. Chem. Res.* **2012**, *51*, 11700−11709.
(21) Sreedhar, B.; Kumar, A. S.; Yada, D. $CuFe_2O_4$ Nanoparticles: A Magnetically Recoverable and Reusable Catalyst for The Synthesis of 5-Substituted 1*H*-Tetrazoles. *Tetrahedron Lett.* **2011**, *52*, 3565−3569.
(22) Yen, H.; Seo, Y.; Guillet-Nicolas, R.; Kaliaguine, S.; Kleitz, F. One-Step-Impregnation Hard Templating Synthesis of High-Surface-Area Nanostructured Mixed Metal Oxides ($NiFe_2O_4$, $CuFe_2O_4$ and Cu/CeO_2). *Chem. Commun.* **2011**, *47*, 10473−10475.
(23) Jin, L.; Qiu, Y.; Deng, H.; Li, W.; Li, H.; Yang, S. Hollow $CuFe_2O_4$ Spheres Encapsulated in Carbon Shells as an Anode Material for Rechargeable Lithium-Ion Batteries. *Electrochim. Acta* **2011**, *56*, 9127−9132.
(24) Zhao, J.; Cheng, Y.; Yan, X.; Sun, D.; Zhu, F.; Xue, Q. Magnetic and Electrochemical Properties of $CuFe_2O_4$ Hollow Fibers Fabricated by Simple Electrospinning and Direct Annealing. *CrystEngComm* **2012**, *14*, 5879−5885.
(25) Zhu, M.; Meng, D.; Wang, C.; Diao, G. Facile Fabrication of Hierarchically Porous $CuFe_2O_4$ Nanospheres with Enhanced Capacitance Property. *ACS Appl. Mater. Interfaces* **2013**, *5*, 6030−6037.
(26) Bomio, M.; Lavela, P.; Tirado, J. L. ^{57}Fe Mossbauer Spectroscopy and Electron Microscopy Study of Metal Extraction From $CuFe_2O_4$ Electrodes in Lithium Cells. *ChemPhysChem* **2007**, *8*, 1999−2007.
(27) Xing, Z.; Ju, Z.; Yang, J.; Xu, H.; Qian, Y. One-Step Solid State Reaction to Selectively Fabricate Cubic and Tetragonal $CuFe_2O_4$ Anode Material for High Power Lithium Ion Batteries. *Electrochim. Acta* **2013**, *102*, 51−57.
(28) Chen, D.; Feng, H.; Li, J. Graphene Oxide: Preparation, Functionalization, and Electrochemical Applications. *Chem. Rev.* **2012**, *112*, 6027−6053.
(29) Chen, J.; Li, C.; Shi, G. Graphene Materials for Electrochemical Capacitors. *J. Phys. Chem. Lett.* **2013**, *4*, 1244−1253.
(30) Ambrosi, A.; Chua, C. K.; Bonanni, A.; Pumera, M. Electrochemistry of Graphene and Related Materials. *Chem. Rev.* **2014**, *114*, 7150−88.
(31) Huang, Y.; Liang, J.; Chen, Y. An Overview of the Applications of Graphene-based Materials in Supercapacitors. *Small* **2012**, *8*, 1805−1834.
(32) Yu, S.; Conte, D. E.; Baek, S.; Lee, D.; Park, S.; Lee, K. J.; Piao, Y.; Sung, Y.; Pinna, N. Structure-Properties Relationship in Iron

DOI: 10.1021/am507014w
ACS Appl. Mater. Interfaces 2015, 7, 2404−2414

Oxide-Reduced Graphene Oxide Nanostructures for Li-Ion Batteries. *Adv. Funct. Mater.* **2013**, *23*, 4293−4305.
(33) Park, S.; Jin, A.; Yu, S.; Ha, J.; Jang, B.; Bong, S.; Woo, S.; Sung, Y.; Piao, Y. In Situ Hydrothermal Synthesis of Mn_3O_4 Nanoparticles on Nitrogen-Doped Graphene as High-Performance Anode Materials for Lithium Ion Batteries. *Electrochim. Acta* **2014**, *120*, 452−459.
(34) Jang, B.; Chae, O. B.; Park, S.; Ha, J.; Oh, S. M.; Na, H. B.; Piao, Y. Solventless Synthesis of an Iron-Oxide/Graphene Nanocomposite and Its Application as an Anode in High-Rate Li-Ion Batteries. *J. Mater. Chem. A* **2013**, *1*, 15442−15446.
(35) Zhang, X.; Sun, X.; Chen, Y.; Zhang, D.; Ma, Y. One-Step Solvothermal Synthesis of Graphene/Mn_3O_4 Nanocomposites and Their Electrochemical Properties for Supercapacitors. *Mater. Lett.* **2012**, *68*, 336−339.
(36) He, G.; Li, J.; Chen, H.; Shi, J.; Sun, X.; Chen, S.; Wang, X. Hydrothermal Preparation of Co_3O_4@Graphene Nanocomposite for Supercapacitor with Enhanced Capacitive Performance. *Mater. Lett.* **2012**, *82*, 61−63.
(37) Allen, M. J.; Tung, V. C.; Kaner, R. B. Honeycomb Carbon: A Review of Graphene. *Chem. Rev.* **2009**, *110*, 132−145.
(38) Huang, X.; Tan, C.; Yin, Z.; Zhang, H. 25th Anniversary Article: Hybrid Nanostructures Based on Two-Dimensional Nanomaterials. *Adv. Mater.* **2014**, *26*, 2185−2204.
(39) Dong, Y.; Cao, C.; Chui, Y. S.; Zapien, J. A. Facile Hydrothermal Synthesis of $CuFeO_2$ Hexagonal Platelets/Rings and Graphene Composites as Anode Materials for Lithium Ion Batteries. *Chem. Commun.* **2014**, *50*, 10151−10154.
(40) Stankovich, S.; Dikin, D. A.; Piner, R. D.; Kohlhaas, K. A.; Kleinhammes, A.; Jia, Y.; Wu, Y.; Nguyen, S. T.; Ruoff, R. S. Synthesis of Graphene-based Nanosheets via Chemical Reduction of Exfoliated Graphite Oxide. *Carbon* **2007**, *45*, 1558−1565.
(41) Hummers, W. S.; Offeman, R. E. Preparation of Graphitic Oxide. *J. Am. Chem. Soc.* **1958**, *80*, 1339−1339.
(42) Si, Y.; Samulski, E. T. Exfoliated Graphene Separated by Platinum Nanoparticles. *Chem. Mater.* **2008**, *20*, 6792−6797.
(43) Nethravathi, C.; Rajamathi, M. Chemically Modified Graphene Sheets Produced by the Solvothermal Reduction of Colloidal Dispersions of Graphite Oxide. *Carbon* **2008**, *46*, 1994−1998.
(44) Dreyer, D. R.; Murali, S.; Zhu, Y.; Ruoff, R. S.; Bielawski, C. W. Reduction of Graphite Oxide Using Alcohols. *J. Mater. Chem.* **2011**, *21*, 3443−3447.
(45) Feng, J.; Su, L.; Ma, Y.; Ren, C.; Guo, Q.; Chen, X. $CuFe_2O_4$ Magnetic Nanoparticles: A Simple and Efficient Catalyst for The Reduction of Nitrophenol. *Chem. Eng. J.* **2013**, *221*, 16−24.
(46) Deng, H.; Chen, H.; Li, H. Synthesis of Crystal MFe_2O_4 (M=Mg, Cu, Ni) Microspheres. *Mater. Chem. Phys.* **2007**, *101*, 509−513.
(47) Chua, C. K.; Pumera, M. Chemical Reduction of Graphene Oxide: A Synthetic Chemistry Viewpoint. *Chem. Soc. Rev.* **2014**, *43*, 291−312.
(48) Tian, J.; Li, H.; Xing, Z.; Wang, L.; Luo, Y.; Asiri, A. M.; Al-Youbi, A. O.; Sun, X. One-Pot Green Hydrothermal Synthesis of CuO−Cu_2O−Cu Nanorod-Decorated Reduced Graphene Oxide Composites and Their Application in Photocurrent Generation. *Catal. Sci. Technol.* **2012**, *2*, 2227−2230.
(49) Zhu, M.; Diao, G. Synthesis of Porous Fe_3O_4 Nanospheres and Its Application for the Catalytic Degradation of Xylenol Orange. *J. Phys. Chem. C* **2011**, *115*, 18923−18934.
(50) Zhu, M.; Wang, Y.; Meng, D.; Qin, X.; Diao, G. Hydrothermal Synthesis of Hematite Nanoparticles and Their Electrochemical Properties. *J. Phys. Chem. C* **2012**, *116*, 16276−16285.
(51) Barlow, D. A.; Baird, J. K.; Su, C. Theory of the von Weimarn Rules Governing the Average Size of Crystals Precipitated from a Supersaturated Solution. *J. Cryst. Growth* **2004**, *264*, 417−423.
(52) Xia, Y.; Yang, P.; Sun, Y.; Wu, Y.; Mayers, B.; Gates, B.; Yin, Y.; Kim, F.; Yan, H. One-Dimensional Nanostructures: Synthesis, Characterization, and Applications. *Adv. Mater.* **2003**, *15*, 353−389.
(53) Xia, Y.; Xiong, Y.; Lim, B.; Skrabalak, S. E. Shape-Controlled Synthesis of Metal Nanocrystals: Simple Chemistry Meets Complex Physics? *Angew. Chem., Int. Ed. Engl.* **2009**, *48*, 60−103.
(54) Chang, H.; Wu, H. Graphene-based Nanocomposites: Preparation, Functionalization, and Energy and Environmental Applications. *Energy Environ. Sci.* **2013**, *6*, 3483.
(55) Chen, Z.; Qin, Y.; Weng, D.; Xiao, Q.; Peng, Y.; Wang, X.; Li, H.; Wei, F.; Lu, Y. Design and Synthesis of Hierarchical Nanowire Composites for Electrochemical Energy Storage. *Adv. Funct. Mater.* **2009**, *19*, 3420−3426.
(56) Stoller, M. D.; Park, S.; Zhu, Y.; An, J.; Ruoff, R. S. Graphene-based Ultracapacitors. *Nano Lett.* **2008**, *8*, 3498−3502.
(57) Zhu, Y.; Murali, S.; Stoller, M. D.; Velamakanni, A.; Piner, R. D.; Ruoff, R. S. Microwave Assisted Exfoliation and Reduction of Graphite Oxide for Ultracapacitors. *Carbon* **2010**, *48*, 2118−2122.
(58) Cao, H.; Zhou, X.; Qin, Z.; Liu, Z. Low-Temperature Preparation of Nitrogen-Doped Graphene for Supercapacitors. *Carbon* **2013**, *56*, 218−223.
(59) You, B.; Wang, L.; Yao, L.; Yang, J. Three Dimensional N-Doped Graphene-CNT Networks for Supercapacitor. *Chem. Commun.* **2013**, *49*, 5016−5018.
(60) Ham, D.; Chang, J.; Pathan, S. H.; Kim, W. Y.; Mane, R. S.; Pawar, B. N.; Joo, O.; Chung, H.; Yoon, M.; Han, S. Electrochemical Capacitive Properties of Spray-Pyrolyzed Copper-Ferrite Thin Films. *Curr. Appl. Phys.* **2009**, *9*, S98−S100.
(61) Giri, S.; Ghosh, D.; Kharitonov, A. P.; Das, C. K. Study of Copper Ferrite Nanowire Formation in Presence of Carbon Nanotubes and Influence of Fluorination on High Performance Supercapacitor Energy Storage Application. *Funct. Mater. Lett.* **2012**, *5*, 1250046.
(62) Zhu, C.; Zhai, J.; Dong, S. Ionic Liquid-Induced Three-dimensional Macroassembly of Graphene and Its Applications in Electrochemical Energy Storage. *Nanoscale* **2014**, *6*, 10077−10083.

DOI: 10.1021/am507014w
ACS Appl. Mater. Interfaces 2015, 7, 2404−2414